

PAPER • OPEN ACCESS

Low frequency $m = 1$ modes during standard and improved confinement scenarios in W7-X

To cite this article: Dario Cipciar *et al* 2025 *Nucl. Fusion* **65** 046010

View the [article online](#) for updates and enhancements.

You may also like

- [Overview of progress in European medium sized tokamaks towards an integrated plasma-edge/wall solution](#)
H. Meyer, T. Eich, M. Beurskens et al.
- [Coherence of turbulent structures with varying drive in stellarator edge plasmas](#)
P Huslage, G Birkenmeier, B Shanahan et al.
- [Overview of the third JET deuterium-tritium campaign](#)
Athina Kappatou, Matteo Baruzzo, Antti Hakola et al.

ARE YOU **STRUGGLING** TO SOURCE MATERIALS?

FIND OUT HOW GOODFELLOW IS HELPING LEAD THE WAY IN MATERIALS RESEARCH

We are proud to support fusion research, supplying materials for groundbreaking advancements since 1946. These include the 2022 LLNL achievement at the National Ignition Facility (NIF). This historic experiment marked the first-ever controlled fusion ignition, producing more energy from the reaction than was used to initiate it.

[Click here to find out more about this story.](#)



SEM image showing Fatigue Striations of a Metal

Fully equipped **accredited research laboratory** to conduct in depth analysis of materials.

Supported by experienced team of materials scientists.

Research and industrial scale production for **new materials** and developing **new capabilities**.

We're excited to partner with you to help drive your research forward. Talk to us today.

 **goodfellow**
ADVANCED MATERIALS





EXPLORE OUR FULL RANGE OF IN STOCK MATERIALS.

- LITHIUM
- TUNGSTEN
- PALLADIUM SILVER ALLOYS
- AND MUCH MORE

SCAN THE QR CODE HERE OR VISIT:
goodfellow.com/nuclearfusionjournal



Low frequency $m = 1$ modes during standard and improved confinement scenarios in W7-X

Dario Cipciar^{1,*} , Carsten Killer¹ , Christian Brandt¹ , Axel Könies¹ , Kian Rahbarnia¹ , Neha Chaudhary¹ , Jiri Adamek² , Olaf Grulke^{1,3}, Henning Thomsen¹, Torsten Stange¹, Ksenia Aleynikova¹ , Matthias Hirsch¹ and the W7-X Team^a

¹ Max-Planck-Institut für Plasmaphysik, Wendelsteinstr. 1, Greifswald 17491, Germany

² Institute of Plasma Physics of the CAS, U Slovanky 2525/1a, Prague 18200, Czech Republic

³ Department of Physics, Technical University of Denmark, Lyngby, Denmark

E-mail: dario.cipciar@ipp.mpg.de

Received 15 October 2024, revised 28 January 2025

Accepted for publication 28 February 2025

Published 11 March 2025



Abstract

In the Wendelstein 7-X stellarator (W7-X), two related global low-frequency electromagnetic oscillations are observed on many diagnostic systems (e.g. plasma stored energy, Mirnov coils, Langmuir probes, etc). The activity is related to the presence of magnetic islands at certain radii. However, in contrast to initial analyses in earlier works, the mode activity is not localized at the magnetic islands, but rather of an $m = 1$ type in the plasma outer-core. We observe a strong cross-correlation between electron temperature fluctuations in the confined plasma region, measured with electron cyclotron emission radiometer, and scrape-off layer fluctuations measured with electric probes. Two limiting cases of the mode activity can be observed based on magnetic configuration. A quasi-continuous (QC) mode case, with frequencies of typically some 100 Hz, is found in configurations that have a 5/5 magnetic island chain at the last closed flux surface (LCFS). The mode frequency is found to increase linearly with the core electron temperature and decrease with increasing electron density. In contrast, for magnetic configurations with the 5/5 magnetic island chain just inside the LCFS, the mode activity becomes bursty and intermittent, exhibiting a crash-event like signature. Although these intermittent events are less frequent, more plasma stored energy is lost per event compared to a period of the QC oscillations. The intermittent oscillations are observable as a broadband modulation in turbulence spectra on most diagnostic systems. The presence of these intermittent bursts goes along with an improved energy confinement in the plasma, superficially resembling H-mode and Edge Localized Modes in tokamaks. A self-limiting process is proposed as an

^a See Grulke *et al* 2024 (<https://doi.org/10.1088/1741-4326/ad2f4d>) for the W7-X Team.

* Author to whom any correspondence should be addressed.



Original Content from this work may be used under the terms of the [Creative Commons Attribution 4.0 licence](https://creativecommons.org/licenses/by/4.0/). Any further distribution of this work must maintain attribution to the author(s) and the title of the work, journal citation and DOI.

explanation of the intermittent oscillations based on observed ejection of particles during each crash event, which leads to steepening of density profiles and temporary suppression of ion temperature gradient turbulence and in turn suppression of turbulence driven $m = 1$ mode causing the crash.

Keywords: W7-X, MHD modes, stellarator, soft x-ray tomography, Langmuir probes, ITG turbulence, ILM

(Some figures may appear in colour only in the online journal)

1. Introduction

Wendelstein 7-X (W7-X) is a steady-state capable stellarator successfully optimized to reach tokamak-like levels of neo-classical transport [1]. However, the optimization of W7-X did not include the turbulent transport, now posing as the main transport channel, limiting the achievable confinement time [2] [3]. The lead microinstability contributing to the turbulent transport in W7-X is expected to be the ion temperature gradient (ITG) turbulence [4]. It was found that a high performance phase (improved confinement times and higher central ion temperatures) can be transiently achieved [5] during plasma scenarios with enhanced density gradients, which suppress ITG turbulence, in agreement with gyrokinetic simulations [6]. The required density gradients can be achieved by core fueling (e.g. via pellet injection or neutral beam fueling) or via reduction of the edge density [5, 7]. Remarkably, in certain magnetic configuration of W7-X featuring large stationary magnetic islands inside the last closed flux surface (LCFS), an improved confinement state was found to be accessible without external core fueling. This state seems to be linked to a magnetic island chain induced $E \times B$ shear flow [8] which is acting as a transport barrier [9, 10]. Relaxations of the transport barrier through Edge Localized Mode (ELM)-reminiscent crashes were observed, but not yet understood [9]. It is thus imperative to investigate the improved confinement scenarios of W7-X with the goal of understanding how to control the microinstabilities and access the high performance scenarios. An investigation of the influence of the magnetic island position was performed using a series of discharges with the iota profile adjusted by changes of the ratio between planar coil currents and non-planar coil currents in order to move the island chain radially inwards or outwards. During such ‘iota scans’ [10] a low-frequency MHD mode activity, visible on nearly all diagnostics (e.g. diamagnetic energy (W_{dia})), was observed to change from quasi-continuous (QC) (harmonic) oscillations to intermittent (ELM-reminiscent) crashes, as the resonant magnetic island chain was moved from the scrape-off layer (SOL) into the confined plasma [11, 12]. As a result of the scan, a configuration with internal magnetic islands positioned radially just inside the LCFS was found to achieve an overall increase of W_{dia} by approximately 20% compared to similar plasmas in different magnetic configurations [5]. Attempts were made to explain the transition between harmonic oscillations and ELM-reminiscent crashes during iota

scans and its impact on confinement, linking the activity to the magnetic island chain under term ‘Island Localized Modes (ILMs)’ [11] or to anomalies in ECR heating deposition (parametric decay instability (PDI)) [13]. However, none of these explanations can account for the observed phenomena and to date there is no theoretical model for the observed phenomena. In this work, we investigate experimentally the mechanism behind such improved confinement scenario and its relation to the intermittent ELM-reminiscent crashes and the QC oscillations, both appearing under standard operating conditions. Using a multi-diagnostic approach, we characterize the dynamics in terms of the spatial scale, the frequencies, the underlying magnetic signature, its influence on the confinement and the role of the magnetic islands. We address the previously proposed explanations in the light of new experimental evidence.

2. Experimental setup

W7-X is a low magnetic shear stellarator with a plasma volume of approximately 30 m^3 and a magnetic field strength of 2.5 T on axis. To make use of the island divertor for plasma exhaust [14], the magnetic field configuration established by the superconducting coils is chosen to have a large order rational at the edge, resulting in a chain of stationary magnetic islands defining the LCFS. These magnetic islands are intersected by 10 discrete island divertor targets, two in each of the five field periods of the machine [15]. The diagnostic systems used in this work are installed in machine ports each in a different module (see figure 1) and will be briefly introduced in this section.

The soft x-ray (SXR) tomography system [16] in W7-X consists of 20 pinhole cameras each equipped with 18 silicon photodiodes, providing 360 lines-of-sight densely covering one out of five triangular-shaped poloidal cross-sections of the plasma vessel. The most relevant contribution to the measured x-ray emissivity S_x is the bremsstrahlung, which is proportional to $S_x \approx n_e^2 T_e^{1/2}$, where n_e is the electron density, T_e is the electron temperature. With temporal resolution limited to a bandwidth of $f = 170 \text{ kHz}$ and the sensitive energy range of photodiodes in a range 1–12 keV, the SXR system is capable of resolving low mode number rotating structures, such as MHD instabilities from the core to the edge, with an average the spatial resolution in the range of $dR \approx dz \approx 4 \text{ cm}$.

The electron cyclotron emission (ECE) heterodyne radiometer provides high temporally resolved (μs) electron temperature profiles along its line-of-sight using 32 channels [17]. For a ‘standard’ configuration, the line-of-sight crosses the ‘bean-shaped’ cross-section, such that, on the low-field side it crosses the magnetic island center and the high-field side the island X-point. The radial locations of the 32 channels are distinguished by measuring X2-mode emission from 120 to 160 GHz.

The Multipurpose Manipulator (MPM) [18] is a reciprocating arm equipped with a probe head carrying 29 electric (Langmuir) probes. These measure spatially detailed plasma parameters of the SOL in the ‘bean-shaped’ cross-section in the outboard mid-plane. Probes were divided into modes of operation as follows: poloidal array of 15 probes measured the floating potential (V_{fl}), used throughout the paper as a proxy for the electron temperature (T_e) with the advantage of high spatial resolution, given by the pin spacing d_{pins} of 4–8 mm; 6 probes were biased at $U_{\text{bias}} = -220\text{ V}$, operating in ‘ion-saturation’ regime, where the ion current ($I_{\text{sat},+}$), related to the local electron density n_e , is measured as a voltage drop on a shunt resistor; 2 triple probes from which the value of local electron temperature (T_e) can be calculated under assumptions of Maxwellian electron energy distribution and spatial homogeneity of plasma parameters on a scale $< 1\text{ cm}$. The poloidal extent of the probe measurement was 11 cm, sufficient to capture a significant part of a magnetic island in the standard island divertor configuration [19]. The probe head was constructed to match the tilt of the average flux surfaces, such that, all of the pins are in a good approximation equidistant from the LCFS. The maximum temporal resolution was limited by a digital low-pass filter with a cutoff frequency of 50 kHz in order to eliminate stray signals at higher frequencies caused by long signal cables. This frequency resolution is sufficient for the purposes of this work.

Other systems relevant for this work are the Mirnov pickup coils [20] measuring the deviations from magnetic equilibrium, ideal for capturing MHD mode activity with a sampling rate of 2 MHz. The poloidal array of Mirnov coils measure the variations in poloidal magnetic field B_{θ} with poloidal mode numbers up to $m \approx 20$ [21]. Continuous and segmented Rogowski coils [22] measure the distribution of toroidal current fluctuations generating a poloidal magnetic flux change Φ_{Rog} in 8 Rogowski segments around a poloidal cross-section. Diamagnetic loops [22] measure magnetic flux changes related to the plasma stored energy W_{dia} , corrected for the contribution of eddy currents in the plasma vessel by a set of correction coils.

3. Experimental observations

In this paper we focus on the low-frequency MHD mode activity of two types: (A) QC oscillations in ‘standard’ magnetic configuration, and (B) as intermittent oscillations in ‘limiter’ magnetic configuration. These two kinds of magnetic

configurations differ in the iota profile: in the ‘standard’ configuration, a 5/5 magnetic island chain is forming the SOL, while in ‘limiter’ configurations the islands are located in the confined plasma volume, just inside the LCFS. The differences in the magnetic configuration between cases (A) and (B) can be visualized using a field line tracing code calculating a vacuum magnetic field for a given set of coil parameters. The resulting Poincaré plots for the cases (A) and (B) are displayed in figures 2(a) and (d), respectively, showing the poloidal cross-sections of magnetic field flux surfaces and the connection length (L_c) of a magnetic field line to the nearest divertor target. In case (A) default (‘standard’) magnetic configuration, the non-planar superconducting coils alone produce a magnetic field with a rotational transform profile that has $\iota_a = n/m = 5/5$ resonance at the edge [10]. Thus, 5 poloidally separated intrinsic magnetic islands exist just outside the LCFS, visible on Poincaré plot figure 2(a). The magnetic islands are locally intersected by toroidally discrete divertor targets, forming the island divertor SOL [23]. Here, the magnetic islands create a broad SOL with L_c ranging from 10 to 500 meters, as indicated by the L_c color map. Moreover, depending on the detailed island position, the central region of the island around the ‘O-point’ [24] might not be intersected by any target, creating a confined region of closed field lines (infinite L_c) in the island center.

In case (B) the coil currents are modified, such that, the ι resonance (and therefore the islands) are positioned further inside the core. Such configurations are called ‘limiter’ configurations, as the divertor plates (or other in-vessel components) merely act as limiters for nested flux surfaces in the edge [10]. The nested flux surfaces than directly intersect the divertor with the LCFS being the last ‘regular’ magnetic flux surface, not intersected by the divertor. In such case the magnetic islands occupy a significant part of the confined plasma volume, while the SOL (region with finite L_c) is rather narrow, as is shown in figure 2(d). In both cases, using the saddle-shaped control coils, placed under each divertor, the edge island sizes can be manipulated.

The time traces of the diamagnetic energy (W_{dia}) depict the nature of the two types of oscillations in terms of shape, amplitude and characteristic repetition rate. The QC oscillations of case (A) have stable amplitude and only slowly varying frequency, while in case (B) oscillations are irregular in amplitude and intermittent, thus will be referred to as ‘crashes’. The amplitude of the W_{dia} oscillations in the diamagnetic signal, shown in figures 2(b) and (e), is typically between 0.1% and 1% per single period, while in case (B) the amplitudes reach up to 5% of W_{dia} loss per event. The two types of oscillations are also clearly observable in the time traces of magnetic flux fluctuations (Φ_{Rog}) measured with segmented Rogowski coils, as well as, in the total toroidal plasma current (I_p) shown as a mean removed fluctuating part (\bar{I}_p) in figures 2(c) and (f). The time traces reveal common traits of the oscillations, such as, the correlation of W_{dia} minima with the deviations (spikes or dips) of the I_p and the inboard-outboard asymmetry observable as a phase shift of π between

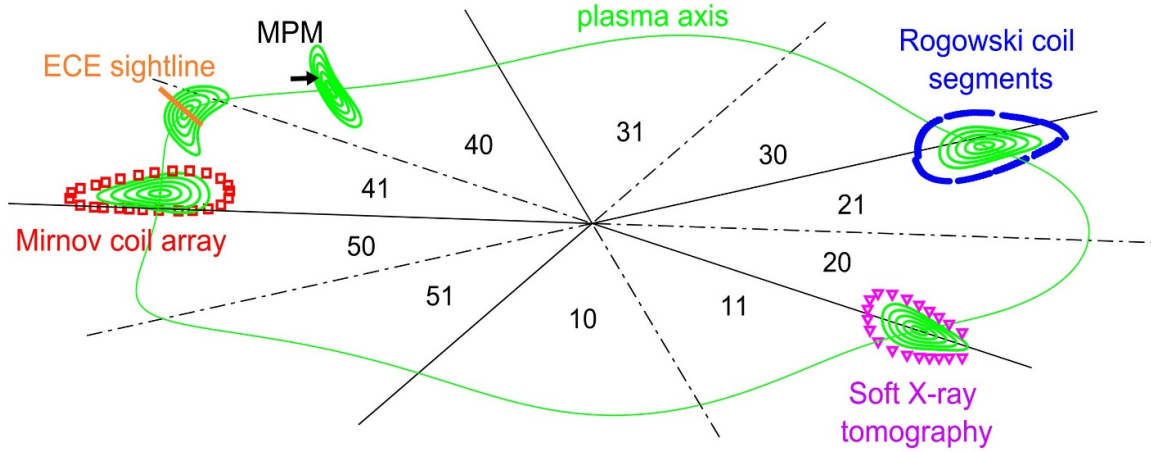


Figure 1. Overview of utilized diagnostic systems and magnetic flux surfaces at their location of measurement for a general magnetic configuration. Black numbers indicate the 10 half-modules of W7-X.

the positive segmented Rogowski induced currents (inboard segment coils) and negative (outboard segment coils). The sign discrepancy of the Rogowski signals (4 outboard coils measure negative Φ_{Rog} and the other 4 inboard coils measure positive Φ_{Rog}) is caused by the dipole character of the neoclassical Pfirsch–Schlüter currents [22].

3.1. QC oscillations

The QC mode is present in multiple magnetic configurations with 5/5 island divertor, but here we only consider the standard configuration as this has the most data available. The most commonly observed frequency is 500 Hz during $P_{\text{ECRH}} = 2\text{ MW}$ and $\bar{n}_e = 1.5 \times 10^{19} \text{ m}^{-3}$ discharges. An example of this behavior was shown in figure 2(b), where each of the periodic oscillations of W_{dia} typically reach 0.1% up to 1% of total W_{dia} . These appear in about 50 ms after the plasma starts and last for the entire duration of the discharge, as long as the plasma parameters remain in the relevant range. In the following we will characterize the activity with multiple diagnostic systems (MPM, ECE, SXR, magnetics), each providing a crucial piece of information about the nature of the oscillations.

3.1.1. Mode activity in the SOL and role of the magnetic islands. The influence of the magnetic island chain on the QC mode activity was previously mentioned [12], where the QC oscillations were suspected to be localized to the islands. In this section the QC oscillations in the SOL islands are examined in detail by measurements using the MPM system, as with the use of probes we are capable of resolving their poloidal and radial structure. From what is known, the magnetic structure of islands, namely the island size, radial position and connection length do affect the shape of the 3D SOL plasma profiles [25, 26]. Therefore, for the study we have selected two different island topologies, both during flat-top phases of discharges in a standard configuration (see figure 2(a)) with near identical plasma parameters ($P_{\text{ECRH}} =$

2 MW , $\bar{n}_e = 3 \times 10^{19} \text{ m}^{-3}$). We compare results of these two cases in two columns of figure 3. Left column refers to the natural magnetic SOL topology, without adding control coil currents, having magnetic islands with a confined region ($L_c = \infty$) at their centers. Right column of figure 3 refers to a magnetic SOL topology with a fully intersected islands, having only finite connection length to the nearest divertor targets. This is achieved by applying $I_{\text{cc}} = (+/-)2.5\text{ kA}$ to (upper/lower) control coils, slightly shifting the islands poloidally and changing their interaction zone with the divertor. In figures 3(a) and (b) the topology of the magnetic field is depicted as a Poincaré plot of magnetic flux surfaces and connection length at the location of MPM. The calculation was done using a magnetic field line tracing code with an inclusion of the on-axis plasma current measured at the instance of the MPM plunge. The connection length in the SOL spans from tens of meters in the ‘target shadow’ region up to infinite in confined regions, not intersecting the divertor targets. The probe plunge, during which the data was recorded, is overlaid as a white polygon, showing the spatial extent of the sampled part of the SOL. The large poloidal extent of the probe allows us to observe distinct features of slowly varying, background ($f < 100\text{ Hz}$) radial and poloidal electric fields related to the presence and topology of a magnetic island [19].

Here we focus on low-frequency 2D SOL fluctuations related to the QC mode activity. The characteristic frequency of the QC oscillations in the SOL is identified with an automated peak identification algorithm utilizing Fast Fourier Transform (FFT) of the floating Langmuir probe signals. The FFT analysis is performed on 20 ms long sub-intervals using a moving window technique with a time step size of 1 ms from each of the floating Langmuir probes. We observe that the frequency identified in each of the sub-intervals remains constant and agrees with a frequency observed in e.g. Rogowski coils. In order to find the source of the QC oscillations, the dominant (highest) peak in the Fourier spectrum is identified in the range of frequencies typical for the QC modes (30–630)

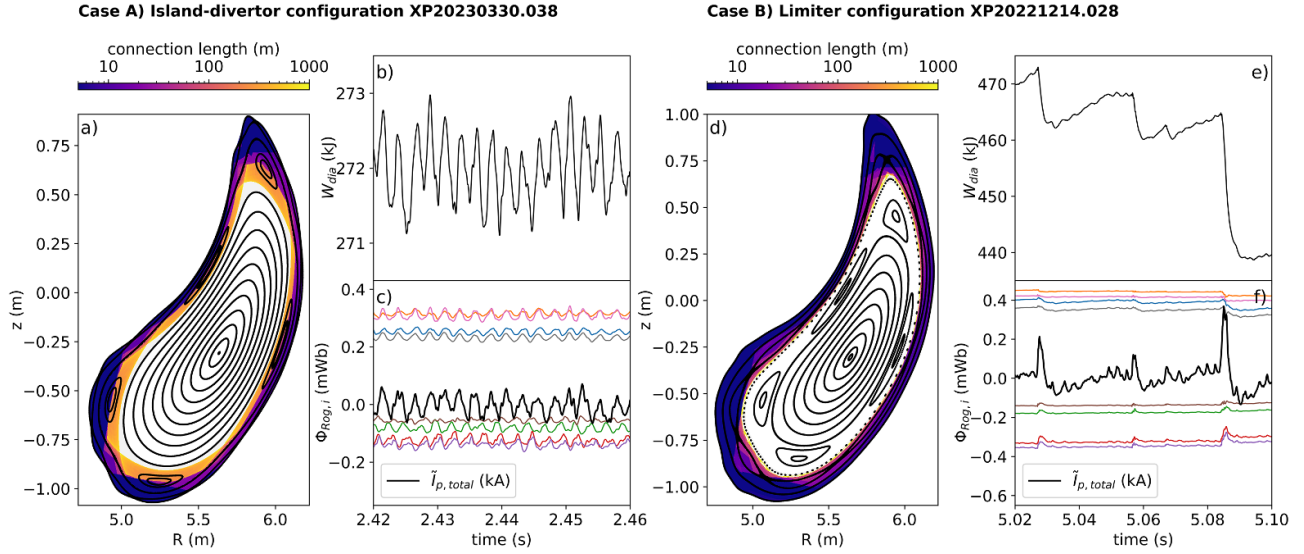


Figure 2. Comparison of oscillations in two magnetic configurations: case (a) standard magnetic configuration and case (b) Limiter magnetic configuration with 5/5 island chain inside the LCFS (dotted line). Shown are the Poincaré plots of magnetic flux surfaces (black contour lines) with connection length between divertor targets (color-coded). Examples of time evolution of dW_{dia}/dt , currents in individual segmented Rogowski coils and the fluctuating part of total plasma current \tilde{I}_p .

Hz and its relative peak prominence estimated in each of the time intervals. The peak prominence measures how much the peak, associated with QC mode, stands out in Fourier spectrum (vertical distance) from the surrounding baseline (lowest contour line) of the signal. As the probe is being plunged into the plasma, from the time intervals we can construct a radial profile of the peak prominence from each Langmuir probe. The result is a 2D (radial-poloidal) heat map of the prominence of the dominant frequency in the Fourier spectrum, shown in figures 3(c) and (d), where the blue-to-red color shading represents an increasing prominence (relative fluctuation level) of the signals at the QC mode frequency. Comparing these two cases we obtain an interesting contradiction. In figure 3(c) the mode prominence is structured radially and poloidally and is clearly peaked in the region of closed field lines in the island center. However, in the figure 3(d), where the island is fully intersected by a divertor target ($L_c = 300$ m), the mode peak prominence profiles are monotonically increasing toward the LCFS, with a local maximum poloidally closer to the island X-point. The clear localization of mode activity to the confined central region of the island would imply that this region is either the origin of the mode or, if the mode is universal, that it is less damped in this region. On the other hand, the monotonic increase of mode activity towards the LCFS, in the island fully intersected case, suggests that the mode is originating inside the LCFS. The later statement can be further strengthened if we make a simple estimate of how much energy is stored in the entire SOL relative to the energy stored in the core. Such estimate of the modulated stored energy during mode activity shows that the mode cannot be purely localized to the SOL or

even parts of it. The energy content W is estimated as:

$$W = \frac{3}{2} \int (n_e T_e + n_i T_i) dV \approx 3Vn\bar{T}, \quad (1)$$

where T_i and T_e is the ion and electron temperature n_i and n_e the ion and electron density and V is the integrated volume. For the sake of obtaining a rough estimate of the volume of the SOL we use simplified geometry, where the SOL is a shell of a torus with $R_{\text{minor}} = (0.50, 0.55)$ m and $R_{\text{major}} = 5.5$ m. In this simple geometry we obtain $V_{\text{SOL}} = 5.7 \text{ m}^3$. Now, if we take the typical SOL plasma parameters $\bar{T} = 20 \text{ eV}$ and $\bar{n} = 5 \times 10^{18} \text{ m}^{-3}$, we obtain $W_{\text{SOL}} = 0.27 \text{ kJ}$. For typical values in the core ($\bar{T} = 1.5 \text{ keV}$ and $\bar{n} = 3 \times 10^{19} \text{ m}^{-3}$) and core volume in this simple toroidal geometry $V_{\text{core}} = 27.1 \text{ m}^3$ we obtain $W_{\text{core}} = 586 \text{ kJ}$. Note, that in this simple estimate we neglect all losses such as radiation, which would decrease the values obtained. From the calculated values we can conclude that even if the entire SOL would disappear, it would cause a relative change of W_{dia} of only 0.05%, which is 10 times less than observed. Also note, that the presence of the probe appears to be non-perturbative for the QC oscillations. The deepest insertion of the probe into SOL during the program XP20230323.11 at $t = 5$ s is not observable in figure 4(b).

The 2D structure of the SOL fluctuations can also be depicted as space-time plots, with the measured quantities V_{fl} and I_{sat} color-coded in the four figures 3(e)–(h). In order to reduce noise the signals were low-pass filtered using a Butterworth filter with a frequency cutoff of 10 kHz (removing noise and broadband turbulence) to visualize the low frequency mode

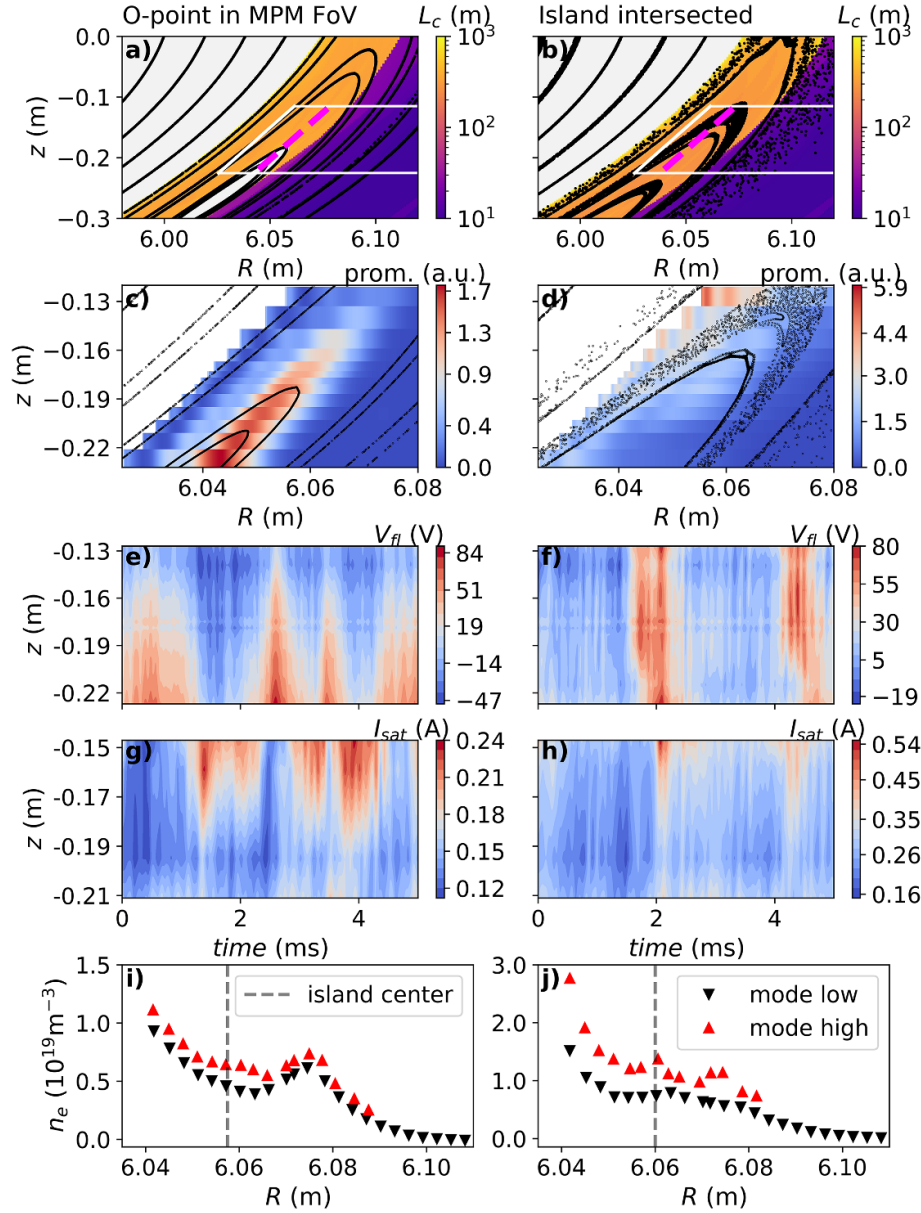


Figure 3. Left column: island ‘O-point’ in MPM field of view: XP20230323037; right column: island intersected by divertor: XP20230323011. (a), (b): Magnetic connection length reconstruction, with overlaid Poincaré plot of field lines, of standard configuration with control coils (a) $I_{cc} = 0$ A and (b) $I_{cc} = (+/-)2.5$ kA to (upper/lower). The precise outline of the probe head plunge is indicated as a white polygon. (c), (d): 2D radial profiles of dominant frequency (≈ 500 Hz) peak prominence in Fourier spectrum of all V_{fl} signals with respect to flux surfaces of the magnetic island. (e–h): Example space-time plots of SOL parameters (V_{fl} and I_{sat}), spanning ≈ 10 cm in a poloidal plane at the location near center of the magnetic island during the QC oscillations. The exact location of the probes with respect to the magnetic island at the moment of this measurement is shown as dashed magenta lines. (i), (j): Radial profiles of electron density conditionally sampled during SOL density peak intervals (red upward triangles) and otherwise (black downward triangles).

structure. Note, the motion of the MPM arm (< 3 mm during the 5 ms interval) can be neglected with respect to the time scale of the oscillations and does not significantly affect the shape of the oscillations. The space-time plots (e) and (g) represent a time instant when the MPM was at the center of the magnetic island, with a confined region ($L_C = \infty$) protruding into the MPM field of view by 5 cm poloidally (see dashed magenta line in figure 3(a)). The space-time plots (f) and (h)

represent an instant when the MPM was at the center of the magnetic island, which was fully intersecting a divertor ($L_C \leq 300$ m) (see dashed magenta line in figure 3(b)). In both cases we observe large scale (> 10 cm poloidally), coherent events of both measured quantities V_{fl} and I_{sat} . These are strongly correlated to the ECE electron temperature fluctuations up to the core channels, as will be shown later in the section 3.1.4. The sudden bursts of I_{sat} signify that during the mode activity

plasma is periodically expelled into the SOL. However, differences can be observed in shape of the V_{fl} events, which indicate significant gradients along z axis in case A (figure 3(e)), while in case B (figure 3(f)) the floating potential is rather uniform along this direction.

The influence of the QC oscillations is also visible as a modulation of the averaged radial profiles of the electron density in the SOL. The perturbation of the background density profiles due to the low-frequency oscillations can be quantified using a conditional sampling technique. This technique is selected due to the fact that MPM cannot measure the entire radial profile as it evolves in time, as it only measures at one radial location at a given time. However, using this technique we can separate the ‘quiescent’ periods from the ‘perturbation’ periods and create the respective average profiles to quantify how much does the density profile deviate from a ‘quiescent’ profile when the QC oscillation has its ‘high’ at any given MPM location. For the density assessment, the upper triple probe is selected for both cases in order to compare regions of similar connection length in the SOL of these two discharges. This is performed by sampling the electron density only during such time intervals when we observe a I_{sat} burst (‘mode high’) and sampling the electron density during such intervals when the events are not present (‘mode low’). The burst (‘mode high’) is defined as $\tilde{I}_{\text{sat}} > \sigma(\tilde{I}_{\text{sat}})$, where σ is the standard deviation and (‘mode low’) otherwise. A radial profile of such conditionally sampled data is constructed by averaging over sub-intervals of each category, during which the probe stays within a range of 3 mm of radial movement. The results in figures 3(i) and (j) show that the bursts increase the SOL density almost exclusively in the center of the magnetic island region (case A, figure 3(i), while in case B) the entire density profile is increased by $\approx 50\%$. Since the experimental programs are very similar in terms of main plasma parameters, such as main field, heating power, plasma density or the core electron temperature, differences in SOL profiles could be attributed to differences in the island inherent $E \times B$ drift effects (as different V_{fl} distributions result in different electric fields) and shear flows forming (or not forming) at the island inner and outer separatrix. Effects of turbulence reduction, due to the presence of island ‘O-point’ shear were previously reported in [27].

Moreover, the frequency of the QC oscillations does not show any correlation with the SOL connection length. The magnetic islands can be either fully intersected by the divertor plates or contain a confined region in their center (‘O-point’) without any influence on the mode frequency, suggesting that the mode originates from the core plasma.

We can summarize a couple of general observations about the mode activity, using the MPM observations in the SOL:

- The frequency of the oscillations observed in the SOL is identical to the frequency observed by core diagnostics (e.g. W_{dia}) and does not change significantly throughout the radial extent of the SOL, irrespective of the size or presence of the ‘O-point’ in the MPM field of view.
- The magnetic islands ‘O-point’, if existing in the SOL magnetic island, causes the SOL oscillation amplitude profiles to be non-monotonic and poloidally non-isotropic forming a local 2D maximum of oscillation amplitude located at the island ‘O-point’.
- The total integrated energy content of an island divertor SOL is expected to be smaller than the observed ΔW_{dia} during 1 average oscillation. Hence, the observed mode activity cannot stem from the SOL.
- The presence of the probe in the magnetic island is non-perturbative to the QC oscillations measured by other diagnostics.

3.1.2. Frequency dependency of the QC oscillations on core parameters.

The oscillations are observable on all segmented Rogowski signals. A spectrogram of signal data by one such coil is shown in figure 4, where its power spectral density (PSD) is color-coded. Figure 4(a) shows a case where the oscillation frequency of the QC mode gradually decreases proportionally to the decreasing core electron temperature ($T_{\text{e, ECE}}$) measured by the ECE system (figure 4, white line).

The spectrogram in figure 4(b) shows an experiment that starts with a phase of $P_{\text{ECRH}} = 4\text{ MW}$, that does not show any mode activity. When the heating power drops to $P_{\text{ECRH}} = 2\text{ MW}$ at $t = 3.5\text{ s}$, the mode activity appears clearly around $f = 400\text{ Hz}$. A temporary interruption of the activity at $t = 6.5\text{ s}$ due to a TESPEL [28] injection is visible, after which the mode gradually resumes its previous frequency.

As figure 4 have already implied, there is a relation of the mode frequency to the core $T_{\text{e, ECE}}$. A survey of total 125 experimental programs was performed, all of which were in the standard magnetic configuration, but with a wide range of parameters, such as, heating power $P_{\text{ECRH}} = (0\text{--}5.5)\text{ MW}$, electron density $\bar{n}_{\text{e}} = (0.2\text{--}1.6) \times 10^{20}\text{ m}^{-3}$, control coil settings, plasma currents $I_{\text{p}} = ((-5)\text{--}10)\text{ A}$ and main gas fueling (helium and hydrogen). From the 125 analyzed discharges 50 exhibited the mode activity. The experimental programs showing this mode activity were found to typically have electron densities $\bar{n}_{\text{e}} < 5 \times 10^{19}\text{ m}^{-3}$ and heating powers $P_{\text{ECRH}} < 4\text{ MW}$. These conditions are only necessary, but not sufficient conditions, i.e. there are plasmas in the mentioned parameter range that do not have the mode. We have not yet been able to identify a systematic difference between the shots with and without mode activity. The fundamental frequencies of the QC oscillations, the width of the PSD peak Δf and its relative prominence above the background level were identified by a Fourier spectrum analysis of the segmented Rogowski coil signals. For the analysis, only peaks within a frequency interval $f = (30\text{--}630\text{ Hz})$ and with a $\Delta f < 40\text{ Hz}$, characteristic for the mode were taken into account. A time interval of 0.2 s was selected, creating a sufficient statistical sample of ≈ 100 oscillation periods for the Fourier analysis, but short enough for the discharge parameters to stay constant. The result of the survey is presented in figure 5 in a frequency versus core

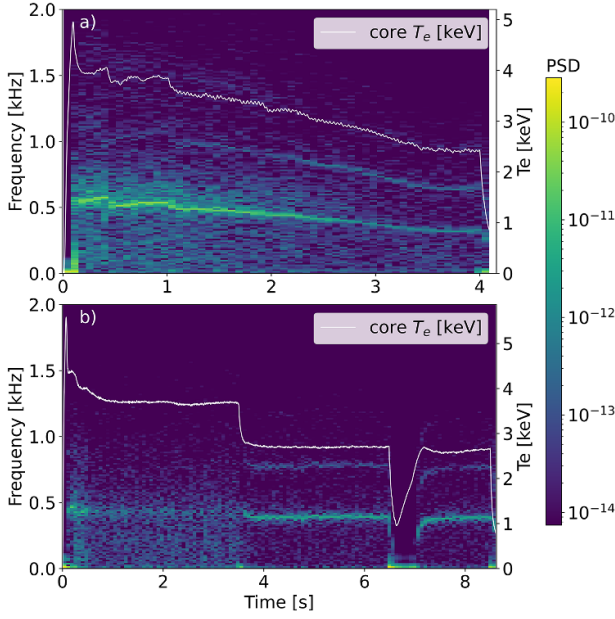


Figure 4. Segmented Rogowski coil spectrograms showing the narrow-band fundamental and harmonic frequencies of the QC oscillations and the time evolution of a core ECE channel $T_{e,ECE}$ (over-plotted as white line) in (a) helium discharge XP20230330.38, (b) hydrogen discharge XP20230323.11.

$T_{e,ECE}$ plot. The data points are color-coded with an average plasma density \bar{n}_e obtained by interferometry. The core $T_{e,ECE}$ was obtained by averaging all available ECE channels measuring in the core plasma $r/a < 0.1$, based on individual channels cold resonance position reconstruction. The mode frequency is observed to have a positive correlation with the core $T_{e,ECE}$ and a negative correlation with the \bar{n}_e . The near linear dependency of the observed frequency on the core T_e was not observed to change significantly between the two main ion species H+ and He+. If the mode would be of Alfvénic nature, a $f \propto 1/\sqrt{\bar{n}_e}$ dependency would be expected with a significant effect of the ion mass. Moreover, we find that, although the mode is strongly related to the core electron temperatures $T_{e,ECE}$ it not clearly related to the heating power P_{ECRH} . At heating powers above 3.5 MW of combined ECRH and NBI, the 500 Hz oscillations tend to be replaced by another type of oscillations, with a more broadband spectrum, $m = 2$ poloidal mode number and a frequency ranging between 1 and 2 kHz, as reported in [29, 30]. Interestingly, near the transition threshold of ≈ 4 MW both types, the 500 Hz and 1–2 kHz oscillations, can be observed simultaneously, even though weakly in the Rogowski coil spectra (not shown here).

3.1.3. The $m = -1$ magnetic structure of QC oscillations.

The QC oscillations are of electromagnetic nature since they are visible on a poloidal array of 31 magnetic pick-up coils (Mirnov coils). The poloidal magnetic structure of the perturbation is visualized with a spatiotemporal cross-correlation analysis shown in figure 6(a), where the spatial coordinate is

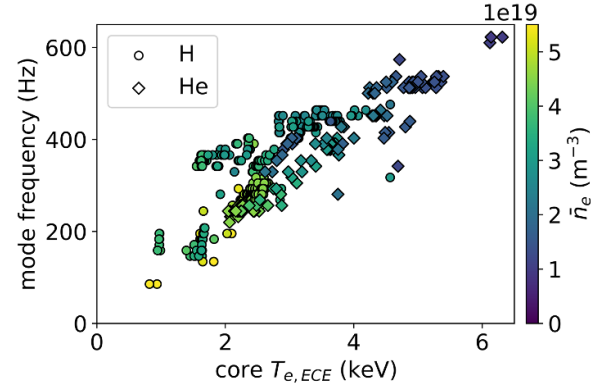


Figure 5. Dependence of the QC oscillation frequency on core $T_{e,ECE}$. The color map represents the average electron density \bar{n}_e .

the poloidal angle θ . A single Mirnov coil signal (horizontal dashed line) is selected as a reference signal and correlated with all 30 other Mirnov coil signals around an entire circumference of the poloidal cross-section. The coils were ordered in such way that θ is increasing in the positive (counterclockwise) direction with a $\theta = 0$ located at the outboard midplane. All of the signals were low-pass filtered with a cutoff frequency 20 kHz, sufficient to capture the $f \approx 500$ Hz of the studied oscillations. The poloidal angle of the reference coil is indicated as a dashed horizontal line. The dominant poloidal mode number can be directly identified as an $m = -1$, since there exists only one cross-correlation maximum at the time delay $\delta t = 0$. The propagation of the magnetic perturbation is in the ion diamagnetic drift $\mathbf{B} \times \nabla p$ (counterclockwise) direction. The relative amplitude of the $m = -1$ mode is visualized by a pictogram in figure 6(b). The circles represent some of the Mirnov coils, with the relative size representing the relative amplitude of the oscillations in the Mirnov coil signals and the color its polarity, showing an up-down asymmetry of the poloidal magnetic field oscillation (reversal of sign) at the instance of measurement.

3.1.4. The radial extent of the $m = -1$ mode. While the Mirnov coil arrays are well suited for studying the poloidal structure of the oscillations in the plasma core, however they do not provide any radial information. As was already shown with electric probe measurements, the QC oscillations lead to strong modulation of the local plasma parameters in the scrape off layer as well. To better understand the underlying radial extent of the oscillations, we make use of a cross-correlation between $T_{e,ECE}$ measured by individual radially spaced channels of the ECE radiometry system on the inboard ‘high-field side’, and the V_{fl} measured by the MPM at a fixed radial position inside the SOL. Note, that the relatively high correlation between the two toroidally separated diagnostic systems during mode activity implies a global character of the oscillations with a low toroidal mode number. In figure 7 the resulting spatiotemporal cross-correlation of the $T_{e,ECE}(r/a)$ and

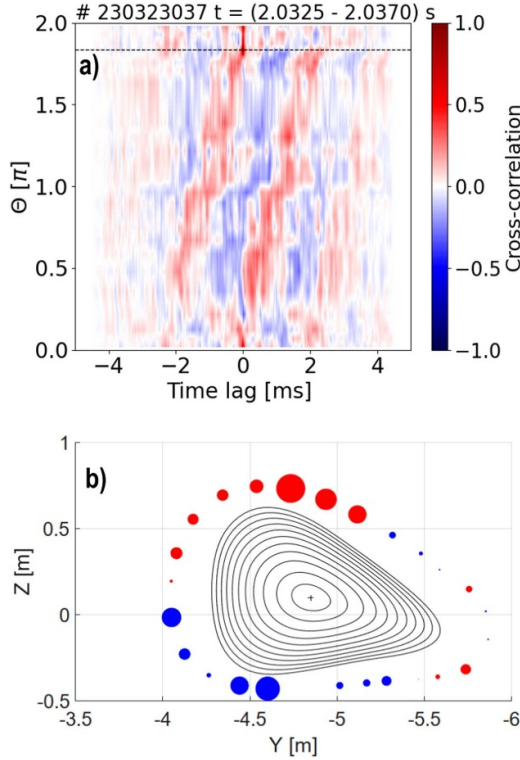


Figure 6. (a) A cross-correlation of all Mirnov coils with a reference coil (dashed line) showing an $m = -1$ structure of the magnetic perturbation during QC oscillations. The tilt of the stripes indicates ion diamagnetic direction (counterclockwise) poloidal propagation. (b) Polarity (color) and relative amplitude (circle size) of the magnetic signal at the mode frequency.

the SOL floating potential (MPM) is depicted. The five regular blue (negative correlation) and red (positive correlation) stripes represent maxima and minima of the cross-correlation during QC oscillations with a frequency of 500 Hz. The tilt of the stripes in the $r/a > 0.55$ region, indicates an outward radial propagation of the temperature perturbation with a radial velocity $v \sim 300 \text{ m s}^{-1}$. A hint of an inward-directed propagation in the $r/a < 0.5$ region is also observable. A distinct change of phase is observed near the estimated position of the LCFS $r/a = 1$ (vertical dashed line).

The radial extent of a significant correlation between MPM and ECE is observed to range from the SOL ($r/a \geq 1$) up to the core (normalized radius $r/a \leq 0.3$). The maximum of the cross-correlation is located near $r/a = 0.55$, roughly where the highest gradient of plasma density is expected [31]. This points at a likely radius of origin of the oscillations and is further supported by the findings from SXR tomography measurements presented in the following section.

Note, that the data presented in the figure 7 is taken from the same discharge, as the data presented in figure 3 case (A). While an analogous result to the one shown in figure 7, can also be obtained from the dataset of the figure 3 case (B). This showcases the fact, that even though the mode prominence in the SOL shows dependency on the SOL L_c

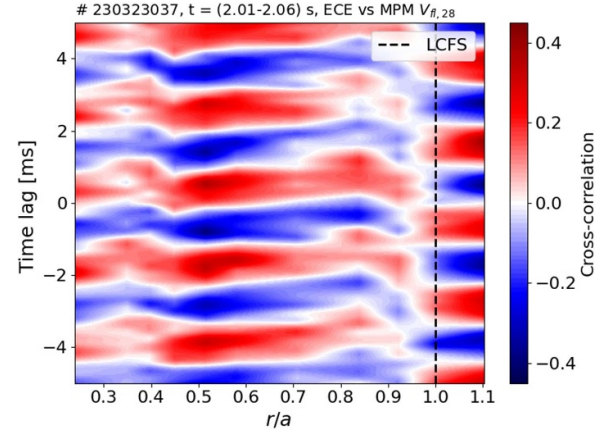


Figure 7. Cross-correlation of several radial ECE channels with one of the MPM floating pins at its deepest insertion, during a discharge phase with active QC oscillations. Highest correlation is located in the gradient region at a normalized radius $r/a = 0.55$. An outward radial propagation is visible in the region $0.4 < r/a < 0.8$, with a distinct phase flip by a π radian located near the LCFS position.

structure, the behavior of the mode in the outer-core plasma remains unchanged. Moreover, when the heating power is increased to e.g. 4 MW in the same magnetic configuration and the QC oscillations disappear (as shown in figure 4(b)), the cross-correlation drops significantly (< 0.1) and no meaningful MPM-ECE cross-correlation pattern appears.

3.1.5. SXR imaging of QC oscillations. Already on spectrograms of raw data of the individual SXR camera lines-of-sight, measuring the line-integrated x-ray radiation, one can observe the frequencies characteristic for the QC oscillations, even with higher harmonics. Just from the fact that SXR diagnostic measures radiation in energy range of 1–12 keV, which is modulated by the QC mode activity, we can infer that the underlying density perturbation is located in the confined plasma. For the regions of plasma with energies below the sensitivity of the detectors the effective signal-to-noise ratio drops rapidly. Such region can be identified, for example, by the ECE radiometry system using T_e profile data. This narrows down the outer boundary for the origin of SXR QC oscillations to $r/a \leq 0.8$. The spatiotemporal structure and the inner boundary of the oscillations can be further detailed by tomographic inversions computed from the measured SXR emissivities. In order to capture the dynamics of the oscillations, the mean value was subtracted from each pixel of the tomogram. Thus, removing the background gradient of the SXR emissivity, while not removing its relative change. In the top subfigure of figure 8(a) time evolution of a mean removed W_{dia} signal and a tomogram pixel are displayed. Four consecutive time points are selected and for each time point a tomogram is plotted in a subplot below. The positive (red) and negative (blue) lobes represent a relative increase (decrease) of SXR emissivity against its mean value. We can observe the QC oscillation as a rotation of SXR emissivity ($S \propto n_e^2 \sqrt{T_e}$) perturbation with

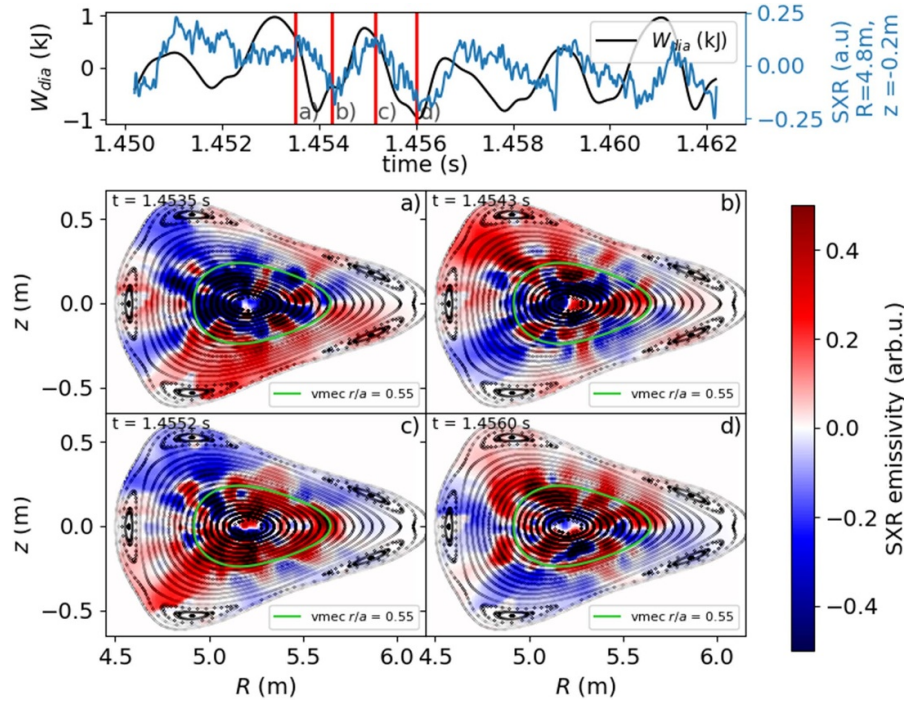


Figure 8. Soft x-ray tomography inversions from program XP20230323.037 at 4 time instances selected as shown in the top insert. The QC oscillations are visible as a counter clockwise rotating $m = -1$ perturbation (fluctuation) extending from approximately $r/a = (0.55 \text{ to } 1)$ in the ‘standard’ configuration. The magnetic reconstruction is shown as a Poincaré plot (black contours) using field line tracing code. A VMEC reconstruction of a magnetic surface at $r/a = 0.55$ is highlighted in green for reference.

$m = -1$ asymmetric structure. An inversion surface defined as $\bar{S}_x(r, t_{\text{after}}) - \bar{S}_x(r, t_{\text{before}}) = 0$ can be identified. Inside of the inversion radius the oscillation of SXR emissivity is in a form of upward ‘spike’, while outside of the radius it forms a downward ‘drop’. Moreover, inside of the inversion radius the $m = -1$ rotation is not observable any longer. An approximate value of the normalized radius r/a of the inversion flux surface can be obtained with a vacuum magnetic field reconstruction using a VMEC code as $r/a = 0.55$ (green surface in figure 8). Thus, the radial extent of the $m = -1$ QC oscillations can be localized using the SXR tomography to the outer core $0.55 \geq r/a \leq 0.8$. It is not clear why the rotating structure is still visible on the tomograms at $r/a \geq 1$, where the signal to noise ratio is rather low, as the T_e in SOL islands is below 50 eV during this particular discharge. Such effect could be caused by impurities increasing SXR radiation or it can simply be an interpolation artefact.

3.2. Intermittent crashes

We will now present results of experiments in the limiter configuration, where the vacuum magnetic field is such that the 5/5 island chain is moved inside the LCFS. In such configurations, intermittent oscillations (crashes) of the plasma stored energy (W_{dia}) typically reach between 1% to 5% of total W_{dia} [32]. An example of this behavior is presented in figure 2(b). The typical duration of a crash is ≈ 2 ms with a typical waiting periods (quiescent phase) of ≈ 20 ms between

major events. The crash rate is not constant during the discharge and can range between $\Delta W_{\text{dia}} = (1\text{--}12) \text{ MJ s}^{-1}$. The heating scenario is not limited to a specific ECR heating power and the crashes occur with the same phenomenology even in purely NBI heated or combined heating discharges.

3.2.1. SXR imaging of a crash event. In figure 9(a) series of tomographic reconstructions capture four key moments of a single crash event as a fluctuation of SXR emissivity. Assuming constant profile of T_e [32] and constant Z_{eff} during the crash event (1 ms), justified by absence of impurity injection, we assume the SXR emissivity as proxy for the electron density. The fluctuating part is obtained, just as in figure 8, by subtracting a mean value of the reconstructed emissivity during a crash event from each pixel separately. This results in removal of the stationary mean background SXR profile, while keeping the fluctuating part. The signal was further filtered by a lowpass filter with a selected bandwidth of 30 kHz.

From the tomography data, a crash event can be described as a sequence of four phases, namely: (a) the initial phase is the plasma quasi equilibrium state before the crash—the SXR emissivity (density) is increased relatively to the mean value in the outer-core region and decreased in the core region; (b) perturbation phase—the evenly radiating outer-core is locally perturbed; (c) rotation phase—the $m = 1$ asymmetric density perturbation starts rotating clock-wise ($T \approx 0.25$ ms or $f \approx 5$ kHz), the W_{dia} soon starts to decrease (d) end phase—the SXR

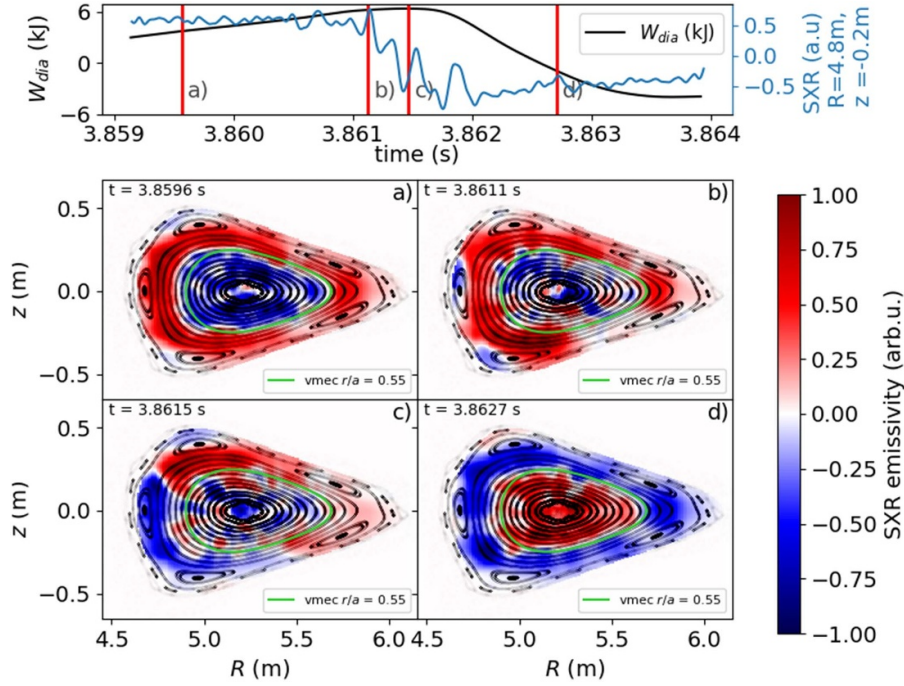


Figure 9. Soft x-ray tomography imaging from a program XP20221214.029 in the limiter configuration showing four key moments of a single crash event as a fluctuation, with respect to the time evolution of W_{dia} . The blue to red color scale represents a below to above average emissivity of a given tomography pixel. The magnetic reconstruction is shown as a Poincaré plot (black contours) using field line tracing code. A magnetic surface at $r/a = 0.55$ is reconstructed using VMEC code and highlighted in green for reference.

emissivity (density) becomes poloidally symmetric with a relative increase in the core and decrease in the edge, the rotation has stopped.

Similarly to QC oscillations, we can identify an inversion surface near $r/a = 0.55$ on the SXR tomograms (highlighted in green in figure 9), where $\bar{S}_x(r, t_{\text{after}}) - \bar{S}_x(r, t_{\text{before}}) = 0$. This contour creates a boundary inside which the $m = 1$ rotation is not observed. Moreover, at the inversion flux surface a ‘downward crash’ of SXR emissivity transitions into an ‘upward pulse’. Similar behavior during crash events was already noted using the ECE radiometry system, where a formation and collapse of an electron temperature pedestal in W7-X limiter configurations was observed during such crash events [9]. The electron temperature pedestal was linked to the presence of magnetic islands as it was located on the inboard side of the island chain in the outer-core region. However, the SXR tomography observation does not imply a formation of an electron density or temperature pedestal prior to the crash event. What it does imply is, that the emissivity in the outer-core region (outside the inversion radius) has decreased by 20% below its pre-crash value via a transport event, involving a rotating $m = 1$ mode. Therefore, the particles must be expelled into the SOL, causing a spike in the SOL transport measured by MPM, which will be discussed in the section 3.2.3. The emissivity inside of the inversion radius (core), has on the other hand increased by 3% above its pre-crash value, indicating an inward particle transport during the rotation phase of the crash event. The increase in core SXR emissivity and

decrease in edge SXR emissivity can be directly observed by comparing average SXR profiles before and after the crash event shown in figure 10. Note, that the crash process still leads to an overall loss of particles and therefore loss of W_{dia} of about 10 kJ which is 2.5% of total stored energy during one such crash.

3.2.2. The $m = 1$ magnetic structure and a radial extent of the mode.

During each crash event the Mirnov coil arrays detect 5 kHz MHD mode activity, while outside the crash intervals the 5 kHz activity is suppressed. A signal analysis is performed using a cross-correlation of a single (reference) Mirnov coil signal (horizontal dashed line) with all other 30 Mirnov coil signals enclosing the circumference of the poloidal cross-section during such crash interval. The result is shown in figure 11(a). Similarly to the QC oscillations, only one cross-correlation maximum at the time delay $\delta t = 0$ can be identified, which signifies the poloidal mode number $m = 1$. The direction of the poloidal rotation, visible as the tilt of the stripes, is in the electron diamagnetic $\mathbf{B} \times \nabla \mathbf{B}$ drift direction (clock-wise), which is in contrast to the $m = -1$ mode observed during the QC oscillations. The difference in rotation direction between the two configurations is currently not understood, as both of the example discharges are in electron root and thus the radial electric field should follow neoclassical electric field expectations, where large differences for the two scenarios are not expected [8].

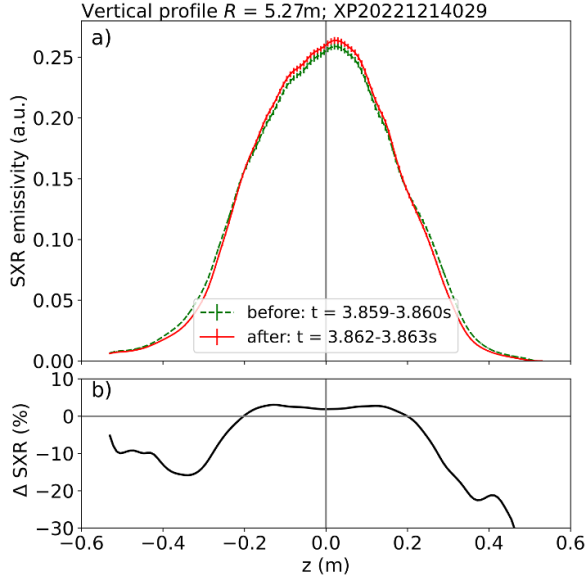


Figure 10. (a) Time averaged (1 ms) soft x-ray emissivity profiles, extracted along central vertical cut of raw tomograms, before (dashed green line) and after the crash event (solid red line); (b) relative change in the profile of SXR emissivity $\Delta S_x = [\bar{S}_x(r, t_{\text{after}}) - \bar{S}_x(r, t_{\text{before}})] / \bar{S}_x(r, t_{\text{before}})$ showing 3% increase in core and 20% decrease in the edge emissivity with an inversion radius at $r/a = 0.55$.

The radial extent of the $m = 1$ mode can be examined in a similar manner as for the QC oscillations, however only during a short time interval during a crash. The radial cross-correlation between the ECE channels and MPM probe in the SOL during a single crash event yields an interesting result shown in figure 11(b). The $m = 1$ mode shows a significant radial correlation extending from the SOL ($r/a \geq 1$) up to the core (normalized radius $r/a \leq 0.3$), similarly to the observation in the standard configuration. However, the distinct phase-flip occurs considerably deeper in the confined plasma ($r/a = 0.8$) as compared to the standard configuration (see figure 7). The radius $r/a = 0.8$ coincides with the position of inner surface of magnetic island chain, which in the case of a limiter configuration is located inside the LCFS (see figure 2(d)). This radial position is also coincident with the island induced W-shaped $E \times B$ shear layers observed with Doppler reflectometry [8], which were previously reported to be acting as transport barriers [9].

3.2.3. Particle transport in the SOL. In the limiter configurations, the magnetic islands do not appear in the SOL. Instead, nested magnetic surfaces intersect divertor plates with connection lengths (L_c) only tens of meters long, see figure 2(b). Thus, in such configurations the SOL is in terms of connection length similar to a limiter tokamak device SOL (apart from the 3D geometry of W7-X).

In figure 12(a) a time trace of dW_{dia}/dt is shown, indicating the presence of a crash event and its relative amplitude. In the figure 12(b) a Morlet wavelet transform of a

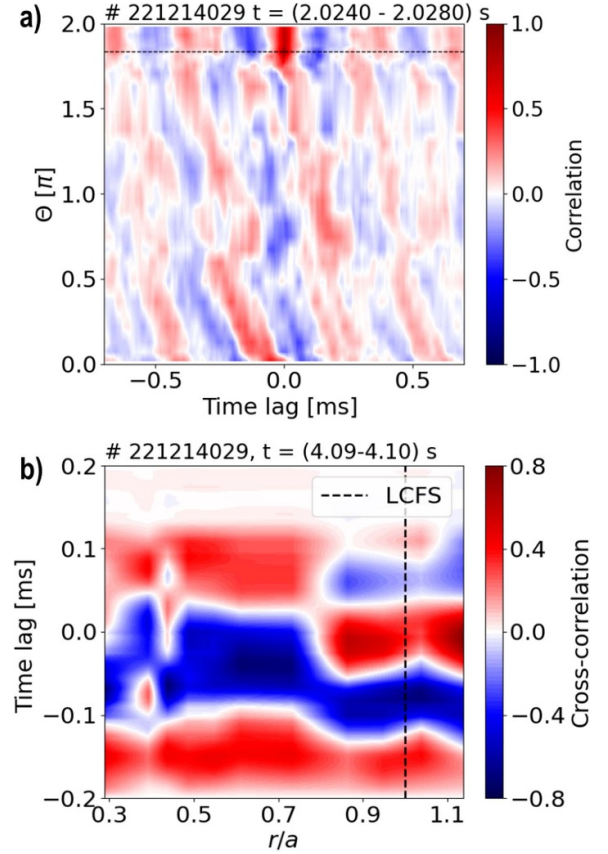


Figure 11. (a) A cross-correlation of a poloidal array of Mirnov coils with a reference coil (dashed line). Showing $m = 1$ structure of the $f = 5$ kHz magnetic oscillations during a crash event and its clockwise poloidal propagation. (b) Cross-correlation of several radial ECE channels with one of the MPM floating pins at its deepest insertion, during a crash event with active $f = 5$ kHz, $m = 1$ oscillations. A phase-flip is observable at $r/a = 0.8$, coinciding with a position of the internal islands. Experimental program XP20221214.029.

Mirnov coil signal shows an increase in the broadband turbulence correlated with the crash intervals indicated on the dW_{dia}/dt time trace. A distinct peak at $f = 5$ kHz, related to the $m = 1$ rotation is seen to appear in magnetic coil spectrum during a crash event. The intervals between the crashes show turbulence suppressed (quiescent) phases without the presence of $m = 1$ mode activity. Since the crash event is observed to reduce the W_{dia} and the outer-core ($0.55 < r/a < 1$) density, the plasma must be also expelled and transported via the SOL to the divertors. Such outward-directed particle transport events in the SOL are indeed experimentally observed to occur simultaneously with the W_{dia} crash events and are shown in figure 12(c). The fluctuating perpendicular particle transport $\Gamma_{r, \text{SOL}}$ was measured by electric probes in the SOL at the deepest insertion of the MPM (≈ 1 cm from LCFS). The particle transport is estimated as $\Gamma_{r, \text{SOL}} = \tilde{n}_e \tilde{v}_r = \tilde{n}_e (\tilde{E}_{\text{pol}} \times B) / B^2$, where $\tilde{E}_{\text{pol}} = \nabla_{\text{pol}} \tilde{\Phi} = (\tilde{\Phi}_{\text{upper probe}} - \tilde{\Phi}_{\text{lower probe}}) / d_{\text{pins}}$, where $\tilde{\Phi}$ is the unperturbed plasma potential and d_{pins} is a poloidal separation of the Langmuir probes.

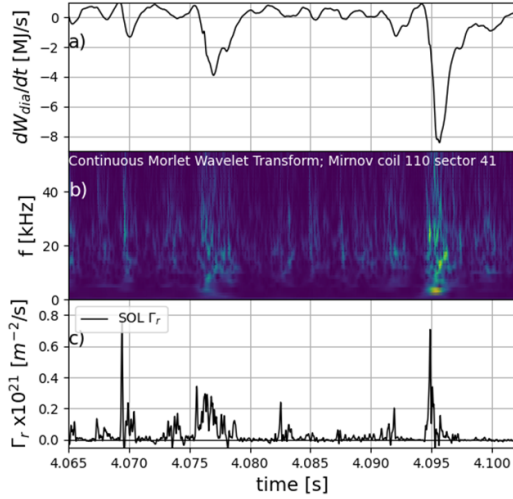


Figure 12. Time traces of (a) W_{dia} derivative, (b) continuous Morlet wavelet spectrum of Mirnov coil signal (c) scrape-off layer perpendicular particle transport. Experimental program XP20221214.029.

Due to technical limitations of the experimental setup, T_e is not measured with sufficient spatial resolution to directly address the influence of the T_e fluctuations between the two probes. However, given the poloidal scale of the observed fluctuations being larger than the size of the probe head and with small time lags between the Langmuir probes, as was shown in figures 3(e) and (f), we can approximate $\nabla_{pol} T_e \approx 0$ at the poloidal distance of $d_{pins} = 8$ mm. In this case the V_{fl} can be used instead of Φ for the computation of poloidal electric field fluctuations \tilde{E}_{pol} , similarly, the I_{sat} is used as a proxy for the density fluctuations $\tilde{n}_e \propto \tilde{I}_{sat}$, neglecting the influence of $\sqrt{T_e}$, as previously done in [33]. At this point it should be noted, that the values of the particle flux can be overestimated when the electron temperature fluctuations are neglected [34].

From the time trace of the particle flux ($\bar{\Gamma}_{r,SOL}$) shown in figure 12(c) it is apparent, that the discharge can be divided into quiescent and transport phases. During the transport phases the outward directed SOL transport is observed to increase in phase with the W_{dia} crashes and with the increase in broadband turbulence. We can observe the direct effect of the broadband turbulence suppression as a reduction of the SOL particle flux during the quiescent intervals. The average turbulent particle flux at the deepest probe insertion is reduced by a factor of 5 during quiescent phases as compared to the average particle flux measured during transport phases. The existence of the turbulence suppressed intervals, where the $m = 1$ mode is not observed, can have an effect on the overall improvement in confinement. This is observed when comparing three self-similar discharges in the limiter configuration in terms of: (a) ECR heating power ($P_{ECRH} = 2$ MW), (b) density ($\bar{n}_e \approx 3 \times 10^{19}$ m⁻³), (c) W_{dia} and (d) the total plasma current (I_p) in figure 13. The main difference between the discharges is the control coil current I_{cc} . We observe that a discharge with

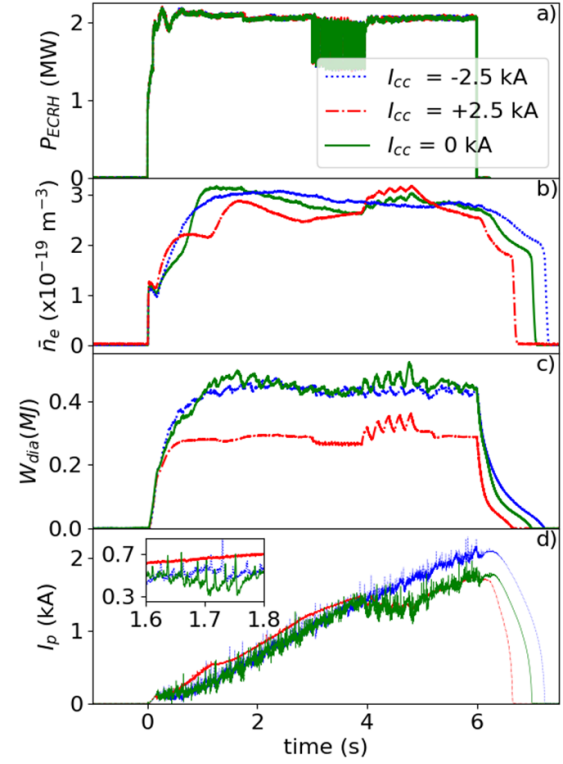


Figure 13. Comparison of main discharge parameters: (a) heating power, (b) average density, (c) W_{dia} (d) I_p with a zoomed-in insert showing the crash behavior detail. Shown are 3 similar limiter configuration discharges with $I_{cc} = -2.5$ kA (blue dotted line, XP20221214.027), $I_{cc} = +2.5$ kA (red dash-dot line, XP20221214.026) and reference $I_{cc} = 0$ kA (green solid line, XP20221214.028).

$I_{cc} = -2500$ A, which significantly decreases the size of the 5/5 islands inside the LCFS, is nearly indistinguishable from a reference discharge $I_{cc} = 0$ A in all of the parameters displayed in figure 13. On the other hand the discharge with $I_{cc} = +2500$ A, where the island size is increased, does not exhibit crashing activity, as can be seen in figure 13(d). While, as shown in figure 13(c), the W_{dia} of the discharge with $I_{cc} = +2500$ A has reached only $\approx 60\%$ W_{dia} of the reference discharge. Such a significant reduction in W_{dia} is not expected, as it was previously reported that the amplitude of the crashes correlates positively with the size of the internal magnetic island and it does not correlate with the plasma stored energy [10]. Moreover, the turbulence suppressed intervals (see figure 12), related to the steepening of the profiles (see figure 9), are not observed to occur in the discharge without the crashes, while only the QC $m = 1$ mode activity is visible in Mirnov coils with $f \approx 2$ kHz during this discharge. From these discharges we can conclude, that the ELM-like crash mechanism may be linked with the improvement in confinement. However, contrary to findings in [10], there seems to be no trivial dependency between the amount of control coil current applied (island size) and the crash amplitude.

4. Discussion

Even though the exact cause of occurrence of the large scale $m = 1$ mode activity cannot be finally identified in this paper, the experimental findings help to narrow-down the possibilities for a drive of the $m = 1$ mode and mechanism of oscillatory or crashing behavior.

Hypotheses providing plausible explanations for the QC oscillations and crashes, which to best of our knowledge can be ruled-out based on findings of this work are:

- Inhibition of ECRH induced PDI [13, 35]. Explanation: PDIs could occur in W7-X due to the non-monotonic density profiles, having a ‘bump’ at the position of magnetic islands, where trapping of upper hybrid waves could locally deposit significant fraction of the input ECRH power into the island. A model was proposed in [13], where the PDI is expected to cause flattening of the density profiles, which would then become more monotonic and periodically self-inhibit the PDI. However, in the limiter configuration the crashes were observed to continue to occur, even when the ECR heating is switched-off and taken-over purely by NBI heating [9]. As the heating scenario change comes without any obvious difference in crashing activity the PDI can be ruled out as the cause of the activity.
- Alfvénic modes. Explanation: The experimentally observed dominant frequencies ranging between 100 to some 1000 Hz of the $m = -1$ and $m = 1$ mode are lower than those of Alfvénic modes (order of some 10 to some 100 kHz). Furthermore, the near-linear dependency of the $m = -1$ mode frequency on the line-averaged electron density does not support an Alfvénic nature of the mode.
- Type-III and type-I ELMs [36, 37]. Explanation: In tokamaks during the transition between L and H-mode, known as an Intermediate (I) phase on AUG [38] or M-mode on JET [39], low-kilohertz harmonic fluctuations occur in form of limit cycle oscillations called ‘dithers’ if irregular [40]. Such oscillations were identified as a type of not fully developed ELMs, which gradually change into ‘bursty’ intermittent type-I ELMs, present during the H-mode phase. The premature ELMs are recognized in tokamaks as type-III ELMs [36], which are characterized by an $m = 1$ up-down asymmetric magnetic activity and a presence of magnetic precursors of the burst activity [37]. Even though the limiter scenario in W7-X features an improvement in confinement accompanied by ELM-reminiscent crashes and the standard scenario features oscillations with similar $m = 1$ magnetic structure as type-III ELMs, there are important differences. For example, the frequency of the type-III ELMs depends rather on edge pedestal pressure and other edge parameters, not on core parameters as was shown in figure 5. Moreover, at higher powers (up to 5 MW ECRH + NBI), unlike the type-III ELMs, the QC oscillations were not observed to transition into type-I ELMs, but rather become only faintly observable in magnetic coil spectrograms and typically with

a broader bandwidth. The radial extent of the density perturbation (figures 8 and 9) and electron temperature perturbation (figures 7 and 11(b)) during the QC oscillations and crashes exclude the possible association with ELMs, as the activity is not strictly edge localized, but rather seem to originate in the outer-core and propagate into the SOL.

- ILMs. Explanation: The oscillation behavior (harmonic or crashing) is tightly related to the position of a magnetic island chain. Thus it was speculated, based on SXR diagnostic line-of-sight observations, that a density perturbation termed ‘ILM’ is localized in the magnetic island and stipulated to propagate with $E \times B$ rotation [11]. However, the tomographic reconstructions based on SXR multi-camera measurements presented in this paper clearly show that the crashes or the QC modes exceed the spatial scale of the magnetic islands. Due to the low plasma temperature in a typical SOL magnetic island with $T_e < 50$ eV, the SXR diagnostic would not be able to resolve any QC oscillations only located there. If the $m = 1$ or $m = -1$ modes would be strictly localized in the island, the MPM-ECE spatiotemporal cross-correlation (figures 7 and 11(b)) would indicate spatially narrow range of significant correlation around $r/a = 1$. Therefore, the term ‘ILM’ used in recent publications seems to be rather inaccurate.
- Radiation induced divertor oscillations. Explanation: Although, H_α filterscopes and gas puff imaging system can see the QC oscillations and the crashes in the emission spectra, a radiation induced oscillations as in [41] or a cyclical transition between attached and detached divertor operation is an unlikely cause, as the total radiated power fraction P_{rad} was typically well below 50% of the input power, thus a stable attached divertor scenario is expected.

After the above listed processes are ruled out as causes of the $m = 1$ mode, it becomes apparent that a more complex mechanism is at play. Data presented in this paper provide a step-forward in understanding and characterization of the $m = 1$ low-frequency modes. However, full understanding can be only achieved with expensive non-linear electromagnetic gyro-kinetic simulations. First simulations [42] and currently ongoing works have already shown that Alfvénic modes with low mode numbers ($m = 1, m = 5, m = 6, \dots$) can be found. These are known to be driven by ITG turbulence [42]. Albeit these modes are at higher (Alfvénic) frequencies, they provide evidence that such mode numbers can be driven unstable by ITG turbulence. These simulations also provide a hint of low frequency activity which, to date, had not been analyzed and therefore motivates future work. Moreover, turbulence driven by both the ion and electron temperature gradients were previously proposed to cause an inward particle flux, missing in neoclassical transport calculations, needed to sustain experimentally measured (weakly peaked) density profiles [43]. Calculations of turbulent flux therein show an inversion radius, where the turbulent transport changes a sign, of $r/a = 0.55$ consistent with the inversion radii of $r/a = 0.55$ observed with

SXR tomography presented here, both in standard and limiter configuration.

From the experimental results discussed in this paper we can learn that the frequency range of the oscillations also does not match the frequency of the Geodesic Acoustic Modes (GAMs), which are heavily damped in W7-X. Instead, the observed frequency range could match the frequencies associated with the zonal flow oscillations related to radial drift of locally trapped particle bounce orbits, sometimes called Mishchenko oscillations [44, 45]. These low frequency zonal flow oscillations may be tied to $m = 1$ activity by geometric coupling and non-linear effects in the spirit employed in [42]. However, we must note that their properties are well known only in the electrostatic limit and thus not directly applicable to our data. Moreover, experimental evidence of zonal flows in limiter configuration is still missing. Thus, we conclude that we currently do not have enough proof to support this hypothesis.

A hypothesis offers if we consider the possibility of ITG turbulence driving the $m = 1$ electromagnetic mode unstable. If true, using the experimental results presented in this paper and in [9], the chain of events during a crash could be outlined as follows:

- ITG turbulence drives large-scale $m = 1$ electromagnetic modes unstable
- These large-scale modes lead to an increased particle transport and a crash of W_{dia} follows
- The crash (transport) event flattens the electron temperature pedestal, as observed in [9], and steepens the density profile (see figure 10), the latter by lowering outer-core density and increasing core density
- ITG turbulence is suppressed by now more peaked density profiles
- Decreased turbulent transport phase follows
- Gradual recovery of W_{dia} along with gradual increase of temperature gradients [9] at constant heating
- ITG turbulence rises again and the process repeats

The model sketched out above might also apply to the QC modes in the standard configuration, if we assume that the $m = 1$ and $m = -1$ modes are driven by the same or at least similar mechanism. Here, the $m = -1$ mode would continuously contribute to transport, however only weakly, insufficient to suddenly transport enough particles needed to suppress the turbulence driving it. Hence, the density profile steepening, which would lead to the improved confinement state cannot spontaneously take place. On the other hand, as has been reported in [5], if the density in a standard magnetic configuration is intentionally peaked, by an advanced heating scheme using both NBI and ECR heating or a pellet injection, confinement improved (high performance) scenario can be accessed. Under such scenario, the drive of the $m = -1$ mode is apparently suppressed, as neither $m = -1$ nor $m = 1$ modes were observed there.

5. Conclusion

The impact of low-order magnetic islands and variation of rotational transform profile on the confinement state is an important factor for development and understanding of high performance scenarios, as well as, the design of a stellarator type reactor. In this paper, we have taken a deeper look at mode activity present during standard and confinement improved plasma scenarios of W7-X with the goal of characterizing the nature, origin and influence of such instabilities.

We have shown the QC oscillations, which occur in island divertor configurations with 5/5 islands with $f = 100\text{--}600$ Hz, are linearly correlated with core T_e and \bar{n}_e in both H and He fueled discharges. The associated density perturbation, observed with SXR tomography, and the magnetic signature of the mode show $m = -1$ asymmetry with a rotation in the ion diamagnetic drift direction. The radial extent of the mode $r/a = (0.3 \text{ to } 1.1)$ excludes the possible association with type-III ELMs. In the island divertor SOL, the mode is present in both long and short connection length regions with a constant frequency. The prominence of the mode in the SOL has a 2D (radial and poloidal) structure and is particularly localized to closed field line regions in the center of magnetic islands.



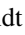


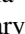


The intermittent crashes, which occur in limiter configurations with confined 5/5 islands, show similar $m = 1$ structure in the SXR tomography and magnetics, however with $f \approx 5$ kHz and rotation in the electron diamagnetic drift direction. Similarly, the vast radial extent of the density perturbation excludes the possible association with ELMs. The crashes of diamagnetic energy are accompanied with phases of increased perpendicular convective transport observed in the SOL with probes and in Mirnov coil signals, as an increase in broadband turbulence. The result of the crash is steepening of the density profiles with $\approx 3\%$ increase in core and $\approx 20\%$ decrease in the edge density with an inversion radius of $r/a = 0.55$. The increased density gradient comes along with a temporary suppression of the $m = 1$ mode and the associated turbulent transport. This process is observed to lead to higher confinement scenarios (30% increase in W_{dia}), as compared to a case where the crashes are suppressed using control coils. The non-trivial effect of the island position and size can be associated with previously observed island induced $E \times B$ shear layer [8], which could be modifying gradients of electron temperature and density and thus the gradient driven turbulence, affecting the crash behavior in amplitude and repetition rate. Although more research is still needed to further clarify the mechanism of the ELM-reminiscent crashes, the presented results provide a basis for further experimental and simulation efforts.

Acknowledgment

This work has been carried out within the framework of the EUROfusion Consortium, funded by the European

Union via the Euratom Research and Training Programme (Grant Agreement No 101052200—EUROfusion). Views and opinions expressed are however those of the author(s) only and do not necessarily reflect those of the European Union or the European Commission. Neither the European Union nor the European Commission can be held responsible for them.

ORCID iDs

Dario Cipciar  <https://orcid.org/0000-0002-3798-9524>
 Carsten Killer  <https://orcid.org/0000-0001-7747-3066>
 Christian Brandt  <https://orcid.org/0000-0002-5455-4629>
 Axel Könies  <https://orcid.org/0000-0003-4306-9000>
 Kian Rahbarnia  <https://orcid.org/0000-0002-5550-1801>
 Neha Chaudhary  <https://orcid.org/0000-0001-5075-2487>
 Jiri Adamek  <https://orcid.org/0000-0001-8562-1233>
 Ksenia Aleynikova  <https://orcid.org/0000-0001-9606-7346>

References

- [1] Helander P. et al 2012 *Plasma Phys. Control. Fusion* **54** 124009
- [2] Geiger B. et al 2019 *Nucl. Fusion* **59** 046009
- [3] Beidler C.D. et al 2021 *Nature* **596** 221–6
- [4] Plunk G.G. et al 2014 *Phys. Plasmas* **21** 032112
- [5] Langenberg A. et al 2024 *Phys. Plasmas* **31** 052502
- [6] Beurskens M.N.A. et al 2021 *Nucl. Fusion* **61** 116072
- [7] Lunsford R. et al 2021 *Phys. Plasmas* **28** 082506
- [8] Estrada T. et al 2021 *Nucl. Fusion* **61** 096011
- [9] Chaudhary N. et al 2024 *Nucl. Fusion* **64** 106038
- [10] Andreeva T. et al 2022 *Nucl. Fusion* **62** 026032
- [11] Wurden G.A. et al 2019 46th EPS Conf. on Plasma Physics (Italy, 8–12 July 2019) p 2.1068 (available at: https://pure.mpg.de/rest/items/item_3168993/component/file_3317968/content)
- [12] Wurden G.A. et al 2018 45th EPS Conf. on Plasma Physics (Prague, Czech Republic, 2–6 July 2018) p 5.1077 (available at: <https://info.fusion.ciemat.es/OCS/EPS2018PAP/pdf/P5.1077.pdf>)
- [13] Tancetti A. et al 2023 *Plasma Phys. Control. Fusion* **65** 015001
- [14] König R. et al 2002 *Plasma Phys. Control. Fusion* **44** 2365
- [15] Sunn Pedersen T. et al 2022 *Nucl. Fusion* **62** 042022
- [16] Brandt C. et al 2020 *Plasma Phys. Control. Fusion* **62** 035010
- [17] Hirsch M. et al 2019 *EPJ Web Conf.* **203** 03007
- [18] Killer C. et al 2022 *J. Instrum.* **17** 03018
- [19] Killer C. et al 2024 *Nucl. Fusion* submitted
- [20] Rahbarnia K. et al 2021 *Plasma Phys. Control. Fusion* **63** 015005
- [21] Büschel C. et al 2024 *Rev. Sci. Instrum.* **95** 023506
- [22] Rahbarnia K. et al 2018 *Nucl. Fusion* **58** 096010
- [23] Feng Y. et al 2011 *Plasma Phys. Control. Fusion* **53** 024009
- [24] Feng Y. (W7-X team) 2022 *Plasma Phys. Control. Fusion* **64** 125012
- [25] Killer C. et al 2019 *Plasma Phys. Control. Fusion* **61** 125014
- [26] Killer C. et al 2019 *Nucl. Fusion* **59** 086013
- [27] Krämer-Flecken A. et al 2019 *Plasma Phys. Control. Fusion* **61** 054003
- [28] Laube R. et al 2020 *Fusion Eng. Des.* **150** 11125
- [29] Ballinger S.B. et al 2021 *Nucl. Mater. Energy* **27** 100967
- [30] Xiang H.M. et al 2023 *Nucl. Fusion* **63** 126050
- [31] Wolf R.C. et al 2017 *Nucl. Fusion* **57** 102020
- [32] Chaudhary N., Hirsch M., Andreeva T., Geiger J., Hoefel U., Rahbarnia K., Wurden G.A. and Wolf R.C. 2023 *EPJ Web Conf.* **277** 03004
- [33] Killer C. et al 2021 *Nucl. Fusion* **61** 096038
- [34] Pfeiffer U. et al 1998 *Contrib. Plasma Phys.* **38** 134–44
- [35] Tancetti A. et al 2022 *Nucl. Fusion* **62** 074003
- [36] Kass T. et al 1998 *Nucl. Fusion* **38** 111
- [37] Birkenmeier G. et al 2016 *Nucl. Fusion* **56** 086009
- [38] Müller S.H. et al 2014 *Phys. Plasmas* **21** 042301
- [39] Réfy D.I. et al 2020 *Nucl. Fusion* **60** 056004
- [40] Zohm H. 1994 *Phys. Rev. Lett.* **72** 222
- [41] Turco F. et al 2024 *Nucl. Fusion* **64** 086008
- [42] Riemann R. et al 2025 *Phys. Rev. Lett.* **134** 025103
- [43] Thienpondt H. et al 2023 *Phys. Rev. Res.* **5** L022053
- [44] Mishchenko A. et al 2008 *Phys. Plasmas* **15** 072309
- [45] Monreal P. et al 2017 *Plasma Phys. Control. Fusion* **59** 065005